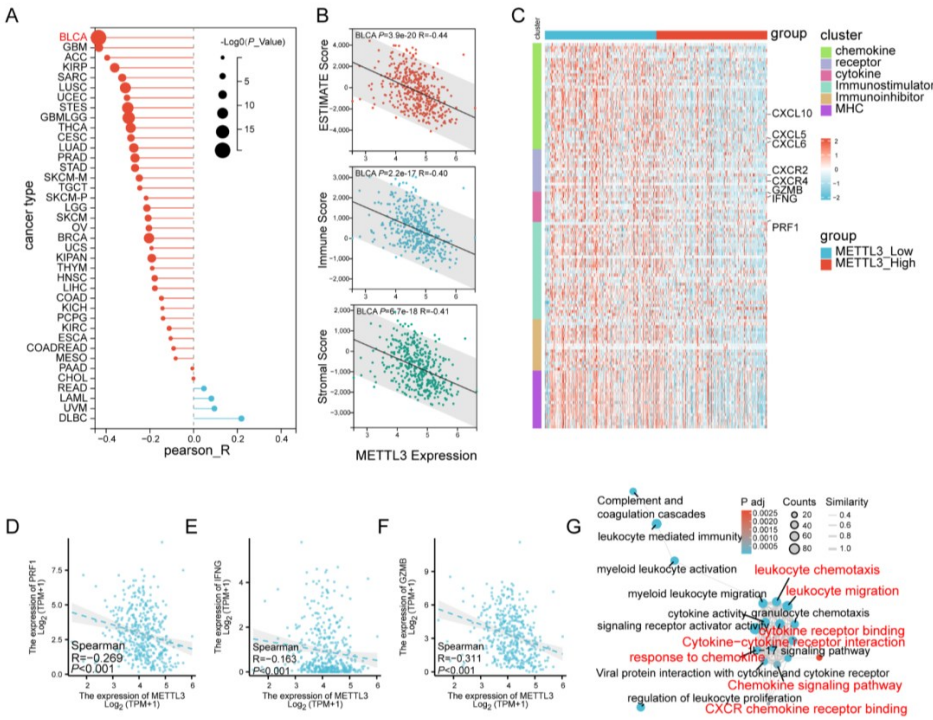

Supplementary Figure S1. **High expression of METTL3 is associated with the formation of an inhibitory immune microenvironment.** (A)Pan-cancer analysis of the correlation between METTL3 expression levels and ESTIMATE Score under the ESTIMATE algorithm; (B) Scatter plots showing the correlation (Pearson correlation) between METTL3 and ESTIMATE Score, Immune Score, and Stromal Score in bladder cancer patients from the TCGA cohort; (C) Heatmap of cytokine, chemokine, and other expression levels in METTL3 high-expression and low-expression groups from the TCGA bladder cancer cohort; Scatter plots showing the correlation between METTL3 expression and functional marker genes of CD8+ T cells in the TCGA bladder cancer cohort: (D) PRF1, (E) IFNG, and (F) GZMB; (G) GO enrichment analysis network plot of differentially expressed genes in high versus low METTL3 expression groups in the TCGA bladder cancer cohort.

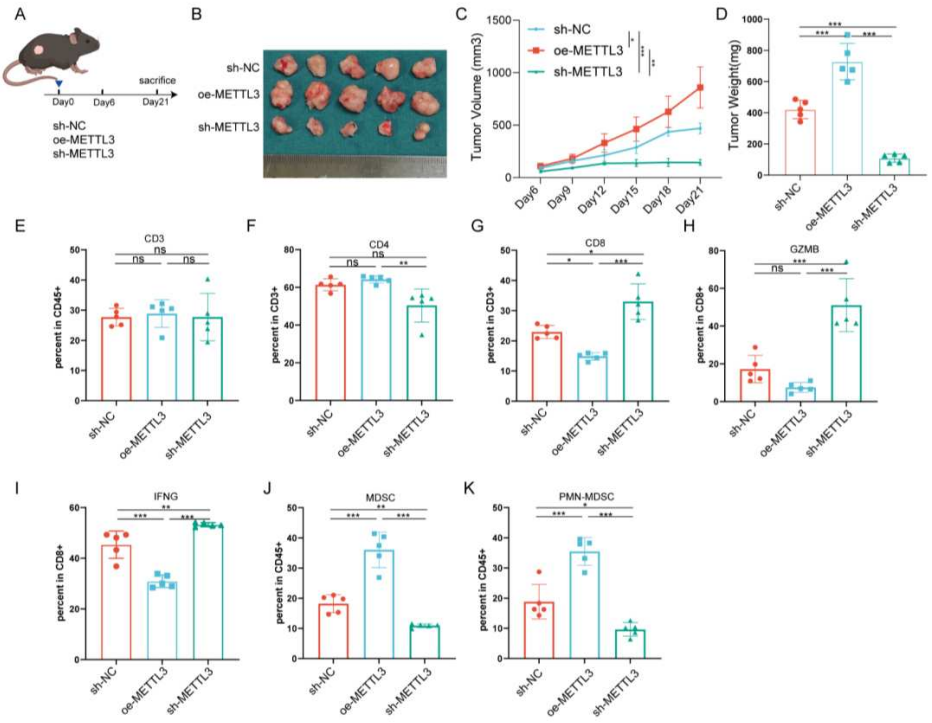

Supplementary Figure S2. Silencing METTL3 inhibits bladder cancer progression in female mice and improves the tumor microenvironment. (A) Schematic of the animal experiment: control, METTL3-silenced, or METTL3-overexpressing MB49 cells were subcutaneously injected into mice, and on day 12, flow cytometry was performed to analyze the tumor immune microenvironment (n=5), along with the assessment of tumor growth in mice (n=5); (B) Images of bladder cancer tumors in mice; (C) Growth curves of bladder cancer tumors in mice; (D) Tumor weights of bladder cancer tumors in mice; (E-K) Analysis results of the immune microenvironment in bladder cancer tumors from mice. *, $P < 0.05$; **, $P < 0.01$; ***, $P < 0.001$.

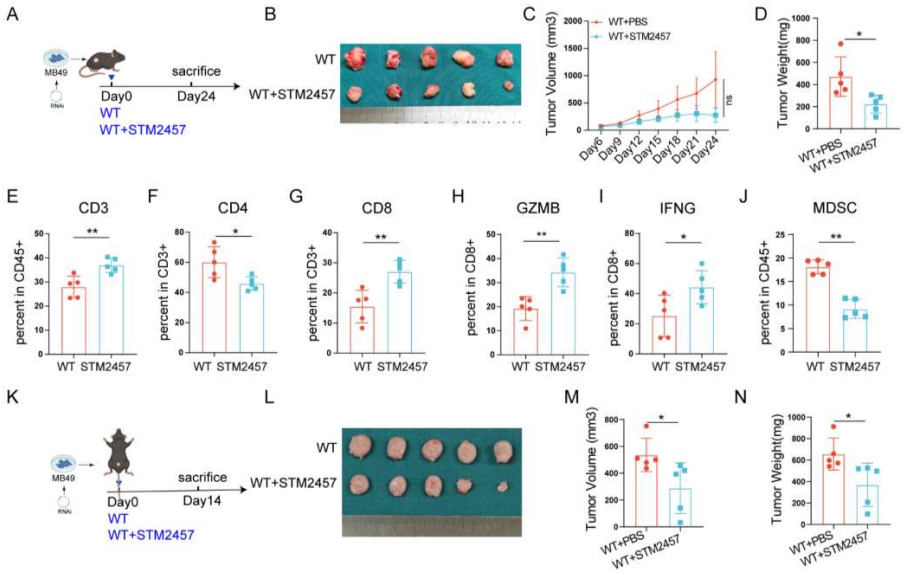

Supplementary Figure S3. STM2457 targets METTL3 to inhibit bladder cancer progression. (A) Animal experiment schematic: wild-type MB49 cells were subcutaneously implanted into the backs of mice, which were then randomly divided into two groups. One group received intratumoral injections of STM2457 (250 μg/tumor, once daily). Tumors were harvested on day 24 (n=5). (B) Images of mouse bladder cancer tumors. (C) Tumor growth curves in mice. (D) Tumor volumes in mice. (E-J) Analysis results of the immune microenvironment in bladder cancer tumors from mice; (K) Animal experiment schematic: wild-type MB49 cells were subcutaneously implanted into the backs of mice, which were then randomly divided into two groups. One group received intraperitoneal injections of STM2457 (25 mg/kg, once daily). Tumors were harvested on day 24 (n=5). (L) Images of mouse bladder cancer tumors. (M) Tumor growth curves in mice. (N) Tumor volumes in mice. ns, no significance; *, $P < 0.05$; **, $P < 0.01$; ***, $P < 0.001$.

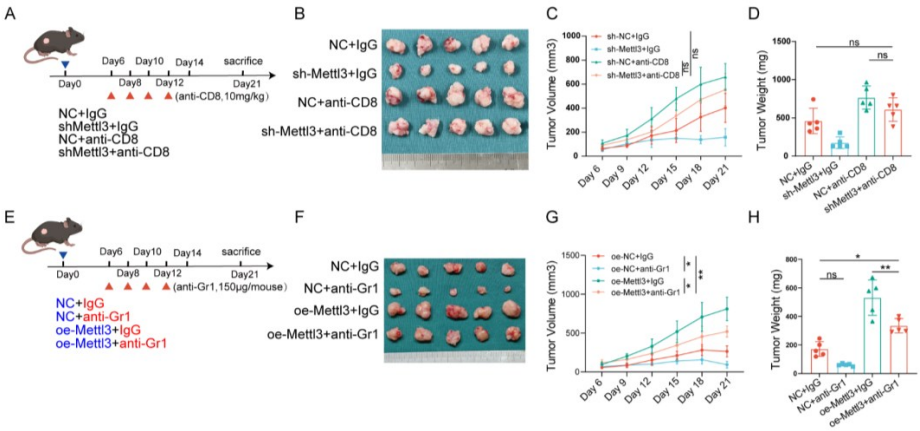

Supplementary Figure S4. The regulation of bladder cancer progression by METTL3 is dependent on CD8+ T cells and MDSCs. (A) Schematic of the animal experiment workflow where control and METTL3-knockdown MB49 stable cell lines were subcutaneously implanted in the backs of mice, followed by treatment with anti-CD8 antibody or IgG antibody starting on day 6 (n=5); (B) Images of mouse bladder cancer tumors; (C) Growth curve of mouse bladder cancer tumors; (D) Weight of mouse bladder cancer tumors; (E) Schematic of the animal experiment workflow where control and METTL3-overexpressing MB49 stable cell lines were subcutaneously implanted in the backs of mice, followed by treatment with the anti-Gr-1 antibody or IgG starting on day 6 (n=5); (F) Images of mouse bladder cancer tumors; (G) Growth curve of mouse bladder cancer tumors; (H) Volume of mouse bladder cancer tumors. ns, no significance; *, $P < 0.05$; **, $P < 0.01$; ***, $P < 0.001$.

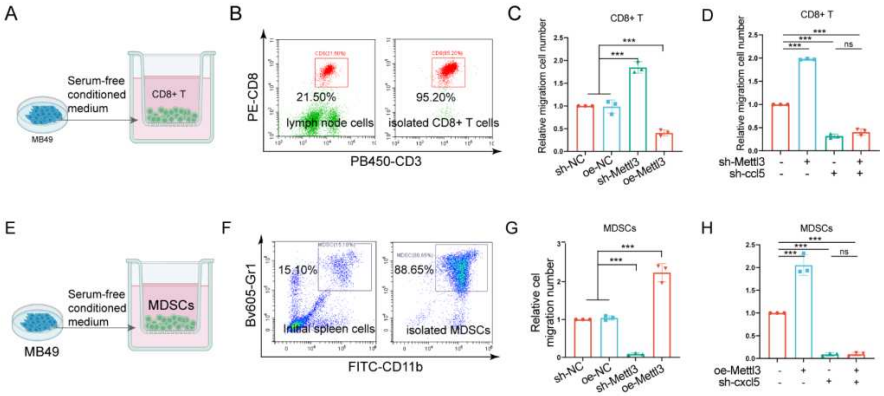

Supplementary Figure S5. METTL3 regulates the chemotaxis of CD8+ T cells and MDSCs by controlling the secretion of CCL5 and CXCL5, respectively. (A) Schematic of CD8+ T cells co-cultured with conditioned media from MB49 cells, where CD8+ T cells were resuspended in serum-free media and cultured in the upper chamber; (B) Flow cytometry analysis of CD8+ T-cell enrichment from mouse lymph node cells; (C) Statistical analysis of CD8+ T-cell chemotaxis after METTL3 overexpression or knockdown; (D) Statistical analysis of CD8+ T-cell chemotaxis after METTL3 knockdown and/or CCL5 interference; (E) Schematic of the MDSC and MB49 cell-conditioned media co-culture experiment, where serum-free conditioned media is placed in the lower chamber and MDSCs are resuspended in serum-free media and placed in the upper chamber; (F) Flow cytometry analysis showing the enrichment of MDSCs from mouse spleen cells; (G) Results of MDSC chemotaxis experiments following METTL3 knockdown or overexpression; (H) MDSC chemotaxis results following METTL3 knockdown and/or CXCL5 knockdown. ns, no significance; *, $P < 0.05$; **, $P < 0.01$; ***, $P < 0.001$.

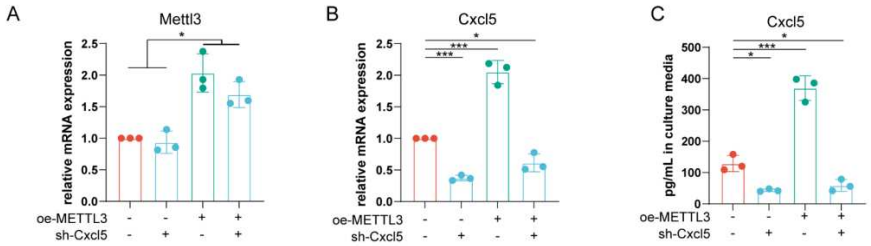

Supplementary Figure S6. Construction of stable CXCL5 knockdown MB49 cell lines. (A-C) Verification of METTL3 and CXCL5 mRNA expression levels and CXCL5 secretion levels in MB49 cell lines with METTL3 overexpression and/or CXCL5 knockdown. ns, no significance; *, $P < 0.05$; **, $P < 0.01$; ***, $P < 0.001$.

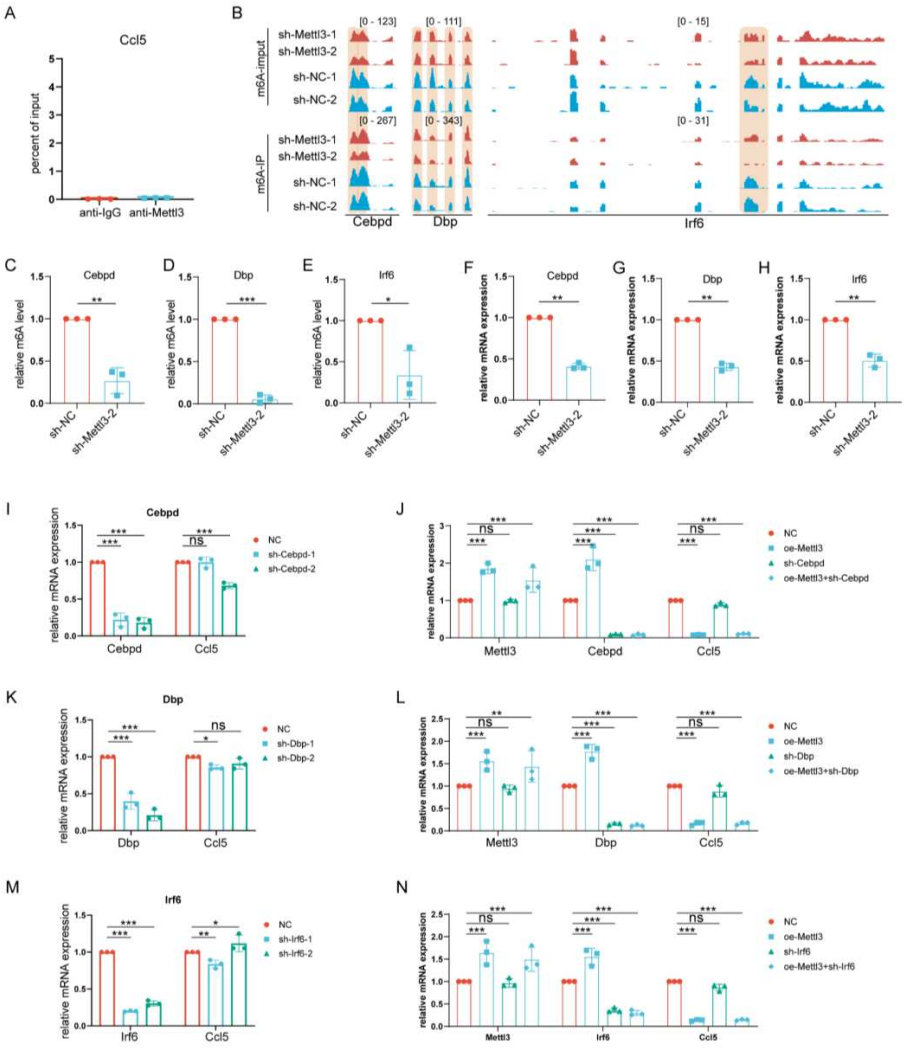

Supplementary Figure S7. The regulation of CCL5 expression by METTL3 is independent of CEBPD, DBP, and IRF6. (A) RIP-qPCR analysis of METTL3 enrichment in CCL5 mRNA in MB49 cells; (B) Peak plot illustrating m6A modification changes in CEBPD, DBP, and IRF6 after METTL3 knockdown; (C-E) MeRIP-qPCR analysis of m6A modification levels of CEBPD, DBP, and IRF6 after METTL3 knockdown in MB49 cells; (F-H) RT-qPCR analysis of CEBPD, DBP, and IRF6 mRNA expression levels following METTL3 knockdown in MB49 cells; (I) RT-qPCR analysis showing changes in CCL5 expression after CEBPD knockdown; (J) RT-qPCR analysis

of CCL5 mRNA expression changes following METTL3 and/or CEBPD knockdown; (K) RT-qPCR analysis showing changes in CCL5 expression after DBP knockdown; (L) RT-qPCR analysis of CCL5 mRNA expression changes following METTL3 and/or DBP knockdown; (M) RT-qPCR analysis showing changes in CCL5 expression after IRF6 knockdown; (N) RT-qPCR analysis of CCL5 mRNA expression changes following METTL3 and/or IRF6 knockdown. ns, no significance; *, $P < 0.05$; **, $P < 0.01$; ***, $P < 0.001$.

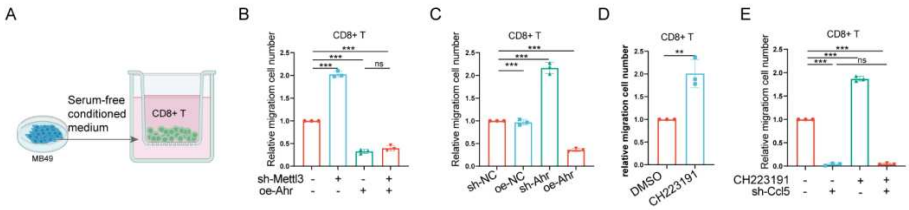

Supplementary Figure S8. AHR is a key gene in METTL3-regulated CD8+ T cell chemotaxis via CCL5. (A) Schematic diagram of cell co-culture; (B) CD8+ T cell chemotaxis after METTL3 knockdown and/or AHR overexpression; (C) CD8+ T cell chemotaxis after AHR knockdown or overexpression; (D) CD8+ T cell chemotaxis after treatment of MB49 cells with the AHR inhibitor CH223191; (E) CD8+ T cell chemotaxis after treatment of MB49 cells with AHR inhibitor CH223191 and/or si-CCL5. ns, no significance; *, $P < 0.05$; **, $P < 0.01$; ***, $P < 0.001$.

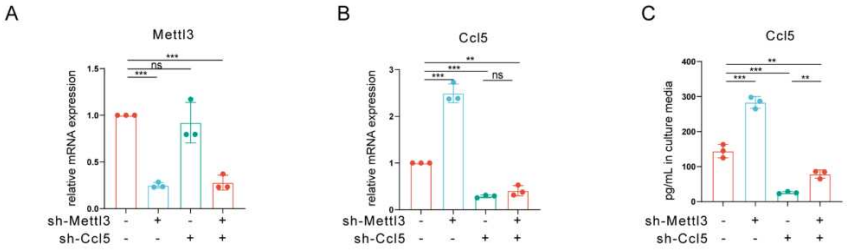

Supplementary Figure S9. Construction of stable CCL5 knockdown MB49 cell lines. (A-C) Verification of METTL3 and CCL5 mRNA expression levels and CCL5 secretion levels in MB49 cell lines with METTL3 knockdown and/or CCL5 knockdown. ns, no significance; *, $P < 0.05$; **, $P < 0.01$; ***, $P < 0.001$.

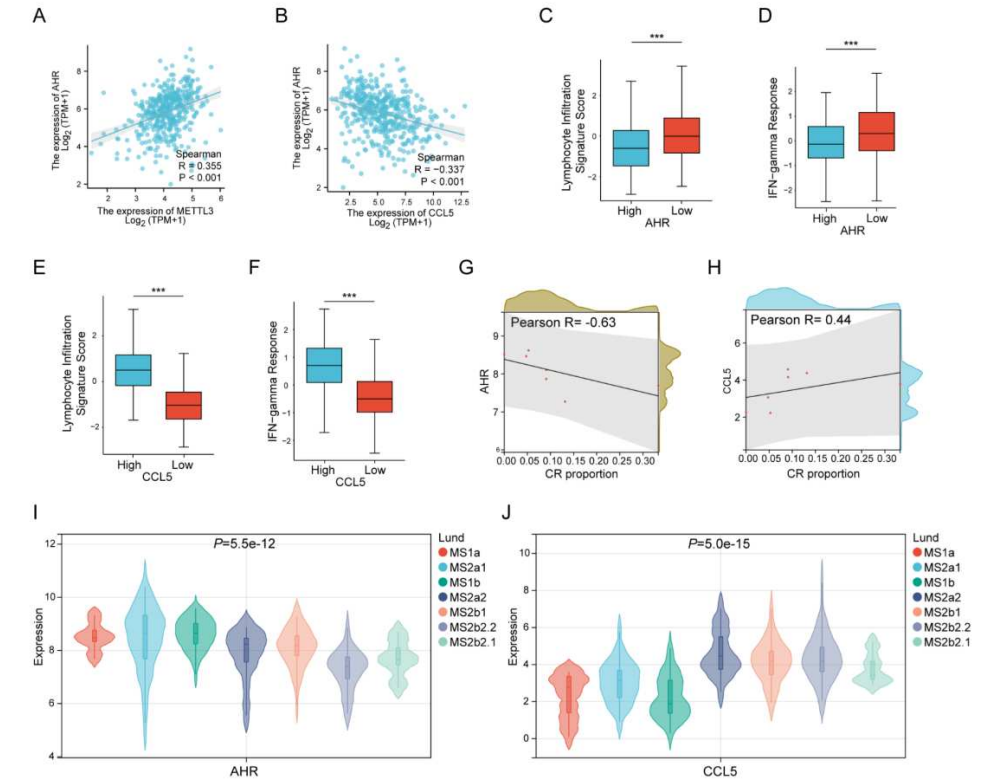

Supplementary Figure S10. METTL3 regulates bladder cancer progression through the AHR-CCL5 axis. (A-B) Correlation scatter plot between AHR and METTL3 or CCL5 expression levels in the TCGA BLCA cohort. Statistical analysis of Lymphocyte Infiltration Signature Score and IFN-gamma Response in the CAMOIP database in patients with different expression levels of (C-D) AHR and (E-F) CCL5. (G-H) Correlation scatter plots of AHR and CCL5 expression levels with the complete response (CR) rate in patients with different Lund subtypes in the Imvigor210 cohort. (I-J) AHR and CCL5 expression levels across different Lund subtypes in the Imvigor210 cohort. *, $P < 0.05$; **, $P < 0.01$; ***, $P < 0.001$.

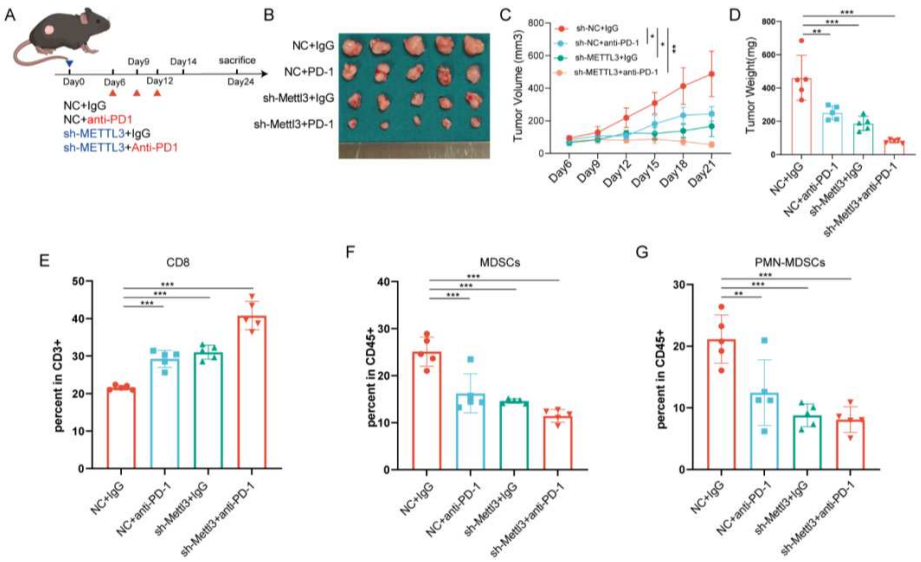

Supplementary Figure S11. Silencing METTL3 enhances anti-PD-1 treatment efficacy in female mice with bladder cancer. (A) Control and METTL3-knockdown MB49 stable cell lines were subcutaneously injected into mice. Anti-PD-1 antibody (200 μg/mouse, every three days) was administered intraperitoneally starting on day 6. Tumors were harvested on day 14 for flow cytometric analysis of the immune microenvironment (n=5) and tumor growth assessment (n=5); (B-D) Images, growth curves, and tumor weights of subcutaneous bladder cancer tumors in mice; (E-G) Flow cytometric analysis of MDSCs and CD8+ T cell infiltration levels in the tumor tissues of mouse bladder cancer. ns, no significance; *, $P < 0.05$; **, $P < 0.01$; ***, $P < 0.001$.